Engineering 43 (2024) 81–88

Contents lists available at ScienceDirect

Engineering

journal homepage: www.elsevier.com/locate/eng

Research
High-End Measuring Instruments—Article

Innovative Inverse-Design Approach for On-Chip Computational Spectrometers: Enhanced Performance and Reliability

Ang Li [a,c], Yifan Wu [a], Gongyuan Zhang [b], Chang Wang [a], Jijun He [a], Yaqi Shi [a], Zongyin Yang [b,*], Shilong Pan [a,*]

[a] National Key Laboratory of Microwave Photonics, Nanjing University of Aeronautics and Astronautics, Nanjing 210016, China
[b] College of Information Science and Electronic Engineering, Zhejiang University, Hangzhou 310058, China
[c] Key Laboratory of Modern Optical Technologies of Ministry of Education of the People's Republic of China, Soochow University, Soochow 215131, China

ARTICLE INFO

Article history:
Received 14 December 2023
Revised 30 June 2024
Accepted 2 July 2024
Available online 26 July 2024

Keywords:
Silicon photonics
Integrated spectrometers
Inverse design

ABSTRACT

Computational spectrometers utilizing disordered structures have emerged as promising solutions for meeting the imperative demand for integrated spectrometers, offering high performance and improved resilience to fabrication variations and temperature fluctuations. However, the current computational spectrometers are impractical because they rely on a brute-force random design approach for disordered structures. This leads to an uncontrollable, non-reproducible, and suboptimal spectrometer performance. In this study, we revolutionize the existing paradigm by introducing a novel inverse design approach for computational spectrometers. By harnessing the power of inverse design, which has traditionally been applied to optimize single devices with simple performance, we successfully adapted it to optimize a complex system comprising multiple correlated components with intricate spectral responses. This approach can be applied to a wide range of structures. We validated this by realizing a spectrometer utilizing a new type of disordered structure based on interferometric effects that exhibits negligible loss and high sensitivity. For a given structure, our approach yielded a remarkable 12-times improvement in the spectral resolution and a four-fold reduction in the cross-correlation between the filters. The resulting spectrometer demonstrated reliable and reproducible performance with the precise determination of structural parameters.

1. Introduction

Integrated single-shot spectrometers offer the advantage of quickly and accurately reconstructing unknown optical spectra, making them suitable for integration into power-sensitive portable devices for real-time monitoring and analysis [1,2]. Silicon photonics, with its rich component library and successful sensing applications, is a promising platform for realizing spectrometers [3]. Conventional integrated single-shot spectrometers rely on narrowband components functioning at different wavelengths; therefore, spectral elements can be spatially split and independently measured [4–6]. This principle is straightforward; however, its high sensitivity to fabrication uncertainties, low spectral resolution, limited bandwidth, and low dynamic range seriously hinder the development of commercial products.

Recently, computational single-shot spectrometers (CSSSs) employing disordered photonic media have emerged as a promising solution to address these challenges [7–14]. The core elements, that is disordered photonic structures (DPSs), aim to generate multiple stochastic samples of the incident spectra. Subsequently, the spectra can be reconstructed by post-processing the sampling results using advanced algorithms. Notably, instead of using multiple disordered photonic media, a single disordered photonic medium with multiple time-domain responses was demonstrated for computational spectrometers [15,16]. Various DPS have been showcased for CSSS, encompassing diverse designs, such as disordered photonic slabs with randomly located etching holes [7,13], quantum dots with random sizes [8,10], and random lasers [11]. Other examples include disordered photonic crystal cavities with random layout [9], random pixelated gratings [17], disordered stratified waveguides with random layers [12], disordered ring resonators of random sizes [18], and random reflectors [19]. Some examples are illustrated in Figs. 1(a)–(c). However, it can be

* Corresponding authors.
E-mail addresses: yangzongyin@zju.edu.cn (Z. Yang), pans@nuaa.edu.cn (S. Pan).

https://doi.org/10.1016/j.eng.2024.07.011
2095-8099/

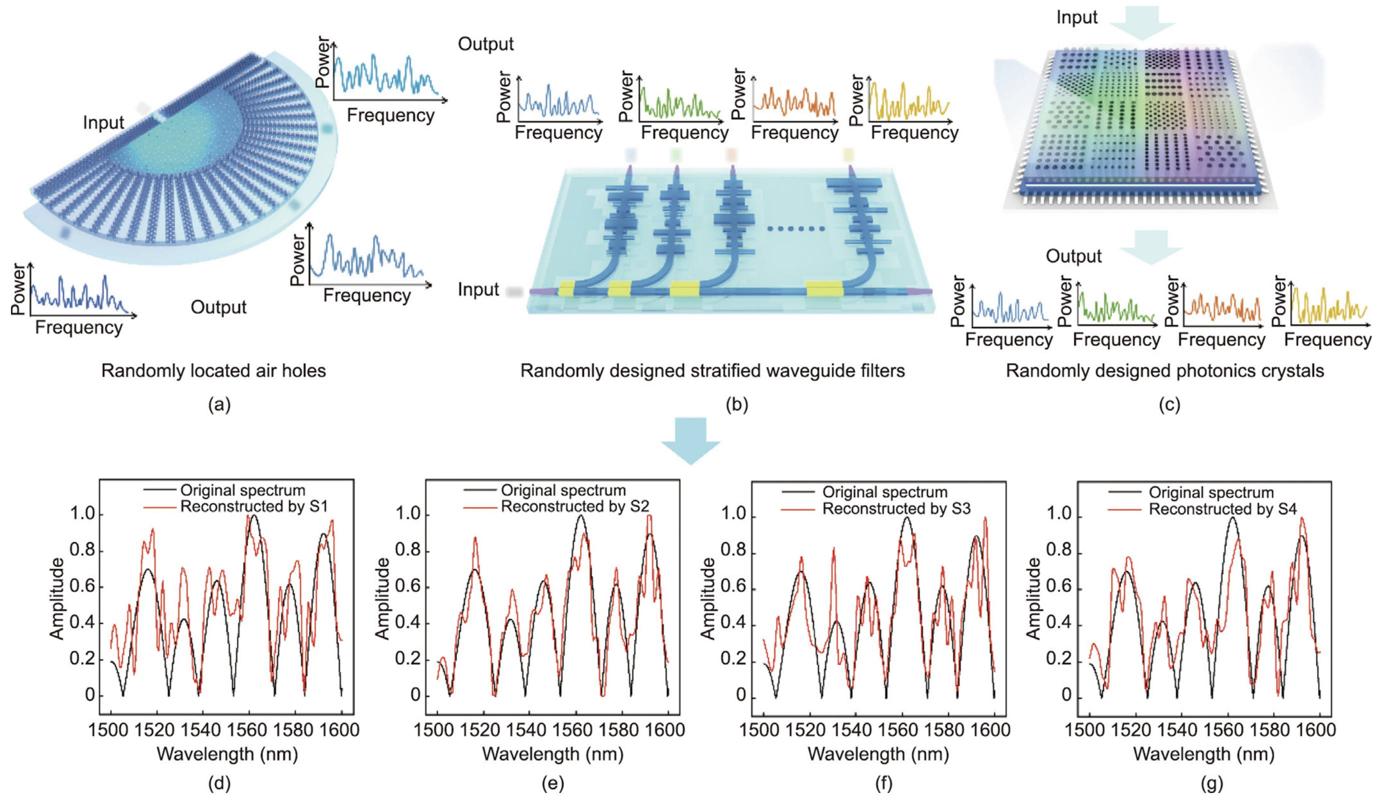

Fig. 1. (a–c) Examples of CSSSs utilizing disordered photonic chips with brute force and random selection of structural parameters; (d–g) spectrum reconstruction by four randomly designed spectrometers (S1–S4).

observed that these DPS are all randomly designed via brute force, with little or no optimization of structural parameters. This significantly limits the development of reliable devices because the brute-force random-design approach inevitably leads to uncontrollable, non-reproducible, and suboptimal performance in spectrometers. Additionally, these DPS designs are associated with several critical detrimental effects, including bandwidth limitations, significant losses, strong back reflections, and a lack of capability for monolithic integration.

In this study, we addressed these critical problems by introducing a reliable design method for a novel type of DPS that can be utilized as a CSSS. The design method uses a bio-inspired inverse algorithm called particle swarm optimization (PSO), which is specifically tailored for computational spectrometers. The novel DPS is fully integrated into a silicon photonics platform, demonstrating its potential for cost-effective mass fabrication. Technically, it relies on interferometric effects rather than scattering or absorption effects and comprises pure waveguide elements with minimal loss. Our design method yielded a remarkable 12-times improvement in spectral resolution and a four-fold reduction in the cross-correlations (CCs) of the DPS spectral responses compared to brute-force random-design methods. Although PSO has been extensively applied to optimize integrated photonic components, it is limited to single devices with simple spectral responses such as waveguide bends [20], splitters [21], grating couplers [22], tapers [23], Bragg gratings [24], and notch filters [25]. To the best of our knowledge, there are no prior reports on its application in systems involving multiple correlated devices with complex spectral responses. This study represents a significant advancement, propelling the readiness of integrated spectrometers for practical applications.

2. Methods

2.1. Problem of disordered photonic media designed in completely random manner

The principle of computational spectrometers using DPS is detailed in Appendix A Section S1. The DPS aims to provide various random spectral responses with low CC. This implies that stochastic sampling of these random spectral responses is linearly independent. The previously demonstrated disordered photonic media for CSSSs were designed using random brute force. Consequently, spectrometer performance is uncontrollable, non-reproducible, and suboptimal. To illustrate this problem better, we designed four spectrometers based on the structure introduced in Ref. [12], which are denoted as S1, S2, S3, and S4, respectively. Each spectrometer comprises 25 randomly designed disordered stratified waveguides. S1 and S2 were designed using identical random generators with Gaussian distributions. S3 was designed using random generators with a uniform distribution. S4 was realized using random generators with a von Mises distribution. These spectrometers were used to reconstruct identical artificial spectra. However, differences were present in terms of reconstruction quality (as shown in Figs. 1(d)–(g)), even for S1 and S2, which were designed using identical random functions. Therefore, a reliable and reproducible design method for disordered photonic chips must be developed to fabricate a practical on-chip CSSS.

2.2. Novel architecture for disordered photonic chip

As previously mentioned, previous CSSS utilized DPS based on effects such as scattering, absorption, and reflection. Thus, some detrimental effects are associated, including high insertion loss, strong back reflections, limited bandwidth, considerable spectral CC, and a lack of monolithic integration ability. We propose leveraging the interference effects to construct a DPS for computational spectrometers. The structure depicted in Fig. 2(a), called the disordered interferometer, can be considered a parallel waveguide configuration with multiple coupling points between the input and output. The output of the structure results from interference among multiple pathways. Each coupling strength (κ), as well as delay lengths (L_1 and L_2) in the upper and lower arms can be engineered as design parameters to customize the transmission spectrum. A disordered interferometer with N coupling points provides 3N design parameters, offering rich design freedom that ensures sufficient randomness and distinction in the spectral response. As a disordered interferometer consists of pure waveguide structures, it exhibits negligible loss, no back reflections, and no bandwidth limitations within a few hundred nanometers. The spectrometer comprising an array of disordered interferometers is shown in Fig. 2(b). A multi-stage Y-junction tree was implemented as a 1 × N power splitter to achieve compact footprint, broad bandwidth, and low power imbalance. The Y-junction was inversely designed according to the instructions reported in Ref. [26]. The inversely-designed Y-junction has a compact footprint of only 1.2 μm × 2.0 μm, a broad bandwidth over 80 nm, and negligible power imbalance. The minimum feature size was greater than 200 nm to ensure high fabrication accuracy using a common fabrication technology. Even if the power-splitting tree introduces a certain power imbalance among its ports, the spectrometer can function normally if the imbalance is within 10 dB [12].

To ensure sufficient randomness, each disordered interferometer requires an adequate number of coupling points. We set the number of coupling points to nine, resulting in 27 design parameters for a single device. The effect of the number of coupling points on the performance of a disordered interferometer is illustrated in Appendix A Fig. S1, and can be found in Appendix A Section S2 and Section S3. Notably, each disordered interferometer should not be designed independently because it is not a standalone device. Instead, they should be designed in a coordinated manner to achieve the desired system-level performance. As each disordered interferometer involves 27 degrees of design freedom, designing

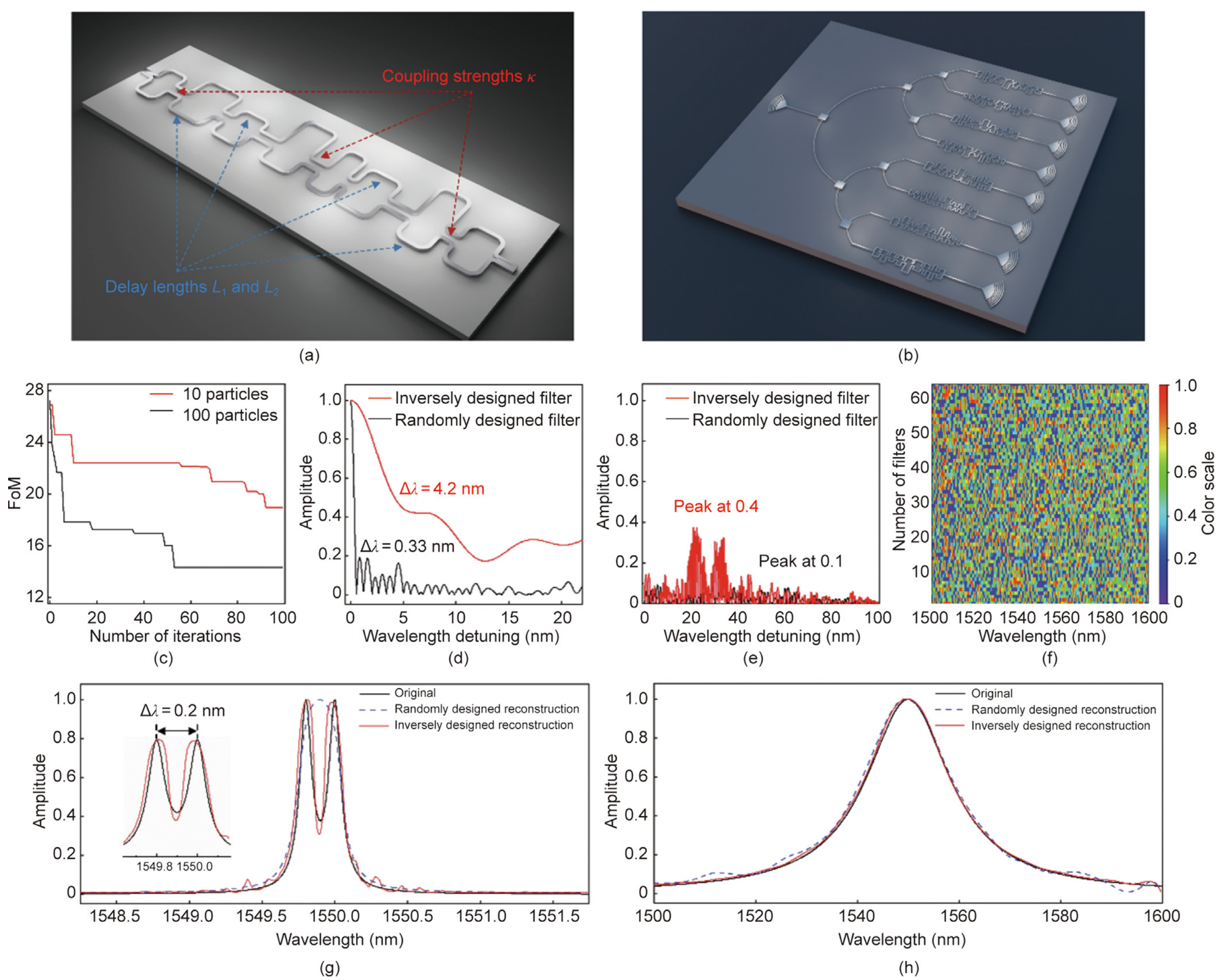

Fig. 2. (a) Schematic of proposed broadband filter. (b) Conceptual layout of single-shot spectrometer comprising an array of broadband filters. (c) The convergence rates of PSO with different numbers of particles. (d) Full-width-half-maximum (FWHM) of autocorrelations (ACs) of randomly and inversely designed filters. (e) CC of spectral responses of randomly and inversely designed filters. (f) The contour plot of the simulated responses of 64 filters. Comparisons of inversely and randomly designed spectrometers in terms of (g) narrow spectrum reconstruction and (h) broad spectrum reconstruction. FoM: figure of merit; Δλ: wavelength resolution.

system-level filters requires hundreds of degrees of freedom. The inverse design method established in this study enables the efficient optimization of these parameters across a large space.

2.3. Inverse design of broadband filters for computational spectrometers

We propose utilizing PSO to perform inverse optimization of this large number of parameters at the system level. PSO is a population-based optimization algorithm inspired by the social behavior of bird flocking or fish schooling [27]. In PSO, a population of particles represents potential solutions to the optimization problem and moves through the search space to search for the optimal solution. In each iteration, each particle updates its position and velocity based on its best position (personal best) and that determined by the swarm (group best). The algorithm also retains the ability to explore randomly to avoid becoming trapped in local optima. The velocity and position are updated using Eqs. (1)–(3), and all the parameters in the PSO are listed and explained in Appendix A Table S1.

$$v_{m,n}^{i+1} = \omega^i v_{m,n}^i + c_1 \mathrm{rand}(p_{\mathrm{best}\,m,n}^i - x_{m,n}^i) + c_2 \mathrm{rand}(g_{\mathrm{best}\,m,n}^i - x_{m,n}^i),\quad -v_{\max} \le v_{m,n}^{i+1} \le v_{\max} \tag{1}$$

$$x_{m,n}^{i+1} = x_{m,n}^i + v_{m,n}^{i+1},\ x_{\min} \le x_{m,n}^{i+1} \le x_{\max} \tag{2}$$

$$\omega^i = \omega_{\max} - (\omega_{\max} - \omega_{\min})\frac{i}{I} \tag{3}$$

where v^i is the velocity in ith iteration, and $v_{\max}$ is the maximum allowed velocity of a particle. ω^i, $\omega_{\max}$, and $\omega_{\min}$ are the inertia weight in ith iteration, maximum inertia weight, and minimum inertia weight during the iteration, respectively. m refers to the mth particle, n is the nth parameter, i is the ith iteration, I is the number of iteration, and c_1 and c_2 are the coefficients for self- and group-cognition, respectively. p_{best} is the personal best found by each particle and g_{best} is the group best found by the entire group. x is the position of the particle (or the value of the parameter); $x_{\max}$ and $x_{\min}$ represent the upper and lower limits of the searching space, respectively; and rand is a random number between 0 and 1.

The equation governing the velocity contains three terms: inertia, self-cognition, and group cognition. Standard PSO uses only Eqs. (1) and (2), as inertia weight ω is fixed. A larger ω indicates a stronger ability to explore a wider area, whereas a smaller ω means a finer search within a small area. When ω is constant, the algorithm may get stuck in local optima and fail to explore new regions of the search space. To better balance exploration and exploitation throughout the search process, we choose a linearly decreasing ω. Additionally, the parameter $v_{\max}$ represents the maximum allowed velocity of a particle, as we used speed-constrained PSO, which is believed to have a higher accuracy and faster convergence rate [26]. A flowchart of the PSO adopted in our design is provided in Appendix A Fig. S2. In each iteration of the algorithm, a figure of merit (FoM) was employed to determine whether the personal and group best solutions were updated. Formulating the FoM for simple devices such as Y-junctions and waveguide bends is relatively straightforward because it primarily focuses on power transmission levels. However, in our case, designing an array of spectral responses with sufficient randomness and a low CC added complexity to the FoM formulation. Instead of simultaneously optimizing the entire system using thousands of parameters, we adopted an approach in which each disordered interferometer was individually designed as part of a correlated design process. To initiate the design process, we designed the first disordered interferometer to minimize autocorrelation (AC) in its spectrum. Therefore, FoM can be expressed as follows:

$$\mathrm{FoM} = \sum_{j=1}^{j=M} \mathrm{AC}_1(\lambda_j) \tag{4}$$

where M is the total number of wavelength points, λ is the wavelength, and j is the jth wavelength point.

By minimizing the AC of the spectrum, we aim to achieve a spectral response that exhibits a low self-correlation, which contributes to the desired randomness in the overall array of disordered interferometers. After completing the design of the first disordered interferometer, we designed the second device. The design objective of the second filter is to minimize the sum of the AC of its spectrum and the CC with the spectrum of the first disordered interferometer.

$$\mathrm{FoM} = \alpha \sum_{j=1}^{j=M} \mathrm{AC}_2(\lambda_j) + \sum_{j=1}^{j=M} \mathrm{CC}_{21}(\lambda_j) \tag{5}$$

where α is the factor adjusting relative weights between AC and CC. The design of the subsequent disordered interferometer follows a similar principle, in which we aim to minimize the sum of the AC of the kth spectrum and that of the CC with the spectra of all previous disordered interferometers:

$$\mathrm{FoM} = \alpha \sum_{j=1}^{j=M} \mathrm{AC}_k(\lambda_j) + \frac{\sum_{j=1}^{j=M} \mathrm{CC}_{k1}(\lambda_j) + \sum_{j=1}^{j=M} \mathrm{CC}_{k2}(\lambda_j) + \copyright\ldots + \sum_{j=1}^{j=M} \mathrm{CC}_{k(k-1)}(\lambda_j)}{k-1} \tag{6}$$

This approach allows us to individually optimize each disordered interferometer while considering its correlations within the system, thereby enabling us to efficiently achieve the desired performance characteristics.

2.4. Simulations of disordered interferometers

The parameters that significantly impact the performance of PSO include M, N, I, c_1, c_2, $\omega_{\max}$, $\omega_{\min}$, and $v_{\max}$. N represents the total number of degrees of design freedom of the device to be optimized, which was 27 in our case. Increasing the number of particles helps find the global optimization more quickly and with greater confidence, albeit at the expense of more computational time. Fig. 2(c) shows that the FoM achieved using ten particles after 100 iterations is significantly higher than that achieved using 100 particles after only ten iterations. Therefore, the number of particles is set to 100. The parameters governing the velocity-updated equation were determined through a thorough literature review and several trial simulations. To ensure convergence, the total number of iterations was set to 60 (as shown in Fig. 2(c)), and the FoM stabilized after approximately 50 iterations. All the PSO parameter settings are summarized in Appendix A Table S2. During the optimization, the coupling ratios are constrained to be within the range of 0.05–0.95, whereas the delay length differences are limited to 0–50 μm. These boundaries define the search space for the PSO algorithm, allowing the parameter space to be explored efficiently to determine the optimal values that satisfy the desired spectral response. The simulated optical span was 1500–1600 nm with a step size of 10 pm. The optimized coupling ratios were converted into waveguide structures based on numerical simulations.

Following this procedure, 64 disordered interferometers are designed. The performance of the first disordered interferometer designed using PSO was compared with that of a randomly designed disordered interferometer in a brute-force manner. The full-width-half-maximum (FWHM) of the AC of the filter designed by PSO is approximately 0.33 nm, whereas that of the disordered interferometer designed randomly is approximately 4.2 nm, as shown in Fig. 2(d). This suggests a 12-fold improvement in spectral resolution when using PSO. The CC between the spectral responses of the second and first disordered interferometers are shown in Fig. 2(e). Notably, using PSO results in a four-fold reduction in the CC compared with the design of the device. These results demonstrate the effectiveness of PSO in optimizing structural parameters to achieve the desired spectral responses. A contour plot of the simulated spectral responses of the 64 disordered interferometers is presented in Fig. 2(f). The disordered interferometer spectral responses exhibit sharp randomness and notable distinctions. In addition, disordered interferometers have been proven to have negligible losses because the peak transmission can reach approximately 1. To further illustrate the value of the inverse design, that is, to better understand the effects of improvement on AC and reduction in CC, we compared the simulated performance of two spectrometers comprising randomly and inversely designed disordered interferometers. As shown in Fig. 2(g), the improvement in AC directly leads to a higher resolution. Two narrow peaks separated by 0.2 nm can be successfully resolved by the inversely designed spectrometer but cannot be captured by the randomly designed spectrometer. Fig. 2(h) shows that the inversely designed spectrometer leads to a higher reconstruction accuracy when reconstructing the broadband spectrum compared with the randomly designed spectrometer, which is attributed to the reduction in CC.

3. Results

A spectrometer consisting of 64 disordered interferometers was fabricated using optical lithography on a 220 nm thick silicon structure layer. The overall footprint of the spectrometer was approximately 4.0 mm × 1.6 mm. Each disordered filter had a footprint of approximately 600 μm × 100 μm. In contrast, the Y-junction tree occupied a space of approximately 4.0 mm × 0.4 mm, which was drastically suppressed because we inversely designed the Y-junction so that it is as small as 1.2 μm × 2.0 μm, over 100 times smaller than a conventional 2 × 2 multimode interferometer (MMI). The chip was packaged with double-fiber arrays permanently attached to grating couplers and a temperature-controller module. The chip was experimentally characterized using two setups, as shown in Fig. 3, which were used to measure the transmission spectra of each channel and to test the spectrum reconstruction quality of the spectrometer.

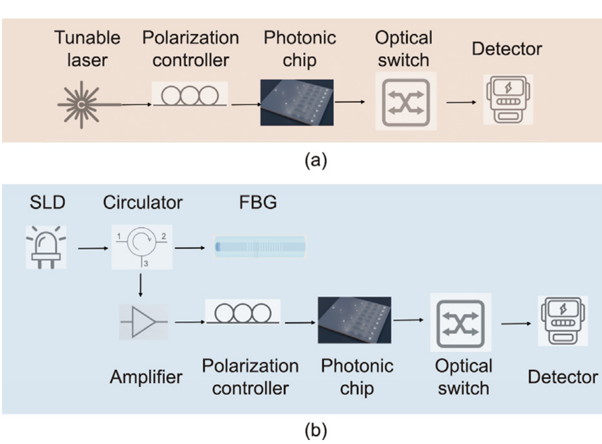

Fig. 3. (a) Setup used to measure static transmission spectra of each spectrometer channel; (b) setup used to test spectrum reconstruction quality of spectrometer. FBG: fiber Bragg grating; SLD: superluminescent laser diode.

The microscopic images of the structure and photographs of the packaged chip are shown in Figs. 4(a) and (b), respectively. The power splitter is composed of a multi-stage Y-junction tree. The compact Y-junction was also inversely designed using PSO to ensure a broad bandwidth and low power imbalances. The chip was characterized using a tunable laser source from 1480 nm (limited by a laser source) to 1600 nm (limited by grating couplers) with a 1 pm step size and a low-noise photodetector. Fiber/chip coupling was achieved by employing vertical grating couplers, with the measured center wavelength being approximately 1525 nm owing to the fabrication variation (designed at 1550 nm) with a 10 dB bandwidth of approximately 80 nm, as shown in Fig. 4(c). The outputs from the fiber arrays were connected to an optical microelectromechanical system (MEMS) switch, which enabled electrical switching between different channels for ease of measurement. Each configuration of the optical MEMS switch takes 100 ms. Therefore, the total data collection requires approximately 6.4 s. In practical applications, 64 photodetectors should be connected to 64 channels so that all the outputs can be collected simultaneously.

Fig. 4(d) shows a contour plot of the transmission spectra of the 64 channels without normalization to the grating couplers, revealing highly random responses. The transmission at longer wavelengths (> 1580 nm) significantly reduced and exhibited strong ripples, which were attributed to the band edges of the grating couplers. To address this limitation, fiber couplers with broader bandwidths can be used to effectively expand the spectrometer bandwidth. The FWHM of each AC are plotted in Fig. 4(e), respectively. Note that AC is calculated after the channel responses are normalized to the spectrum of the grating couplers. Notably, each channel exhibits a narrow FWHM of approximately 0.4 nm, which is consistent with simulations. This small discrepancy can be attributed to the presence of parasitic reflections and fabrication variations, which resulted in slight variations in the FWHMs values. The 64 channels produced over 2000 CC, making it impractical to plot all of them. Fig. 4(f) illustrates a few exemplary CC, showing that the CC maintains a consistently low level across the 120 nm optical span, indicating distinct differences between the channel spectra. The peak amplitudes of the 2016 CCs of the spectral responses of the 64 channels are plotted in Appendix A Fig. S3 and Section S4.

To evaluate the spectral resolution of our spectrometer, we generated spectra using a broadband superluminescent diode source (110 nm 3 dB bandwidth at approximately 1550 nm) and fiber Bragg gratings (FBGs) with varying passbands at different wavelengths. The FBG reflection spectra were transmitted to a chip for reconstruction. The entire optical span, from 1480 to 1580 nm, was digitized to 5000 points using the CVX algorithm implemented in MATLAB (MathWorks, USA). CVX is well known for solving convex underdetermined problems and has been frequently applied in computational spectrometers [9,12,28]. More details regarding the reconstruction algorithms deserve an in-depth study; however, they have already been extensively studied [14,29,30]. In addition, our previous work provided significant details regarding the principle of choosing a reconstruction algorithm [12]. During the reconstruction, the optical span from 1480 to 1580 nm was represented by 5000 data points. Each reconstruction requires approximately three minutes on a workstation with a 16-core Intel®Core™ I9 central processing unit (CPU) and 64 GB random access memory (RAM). The reconstruction time is strongly dependent on the number of data points; thus, for real applications such as glucose analysis, the number of data points can be reduced to less than 100, and the reconstruction time can be greatly suppressed. The results of the reconstruction at 1500, 1525, 1550, and 1580 nm with a 0.2 nm bandwidth are depicted in Fig. 5(a). The passbands at 1500, 1525, and 1550 nm were accurately

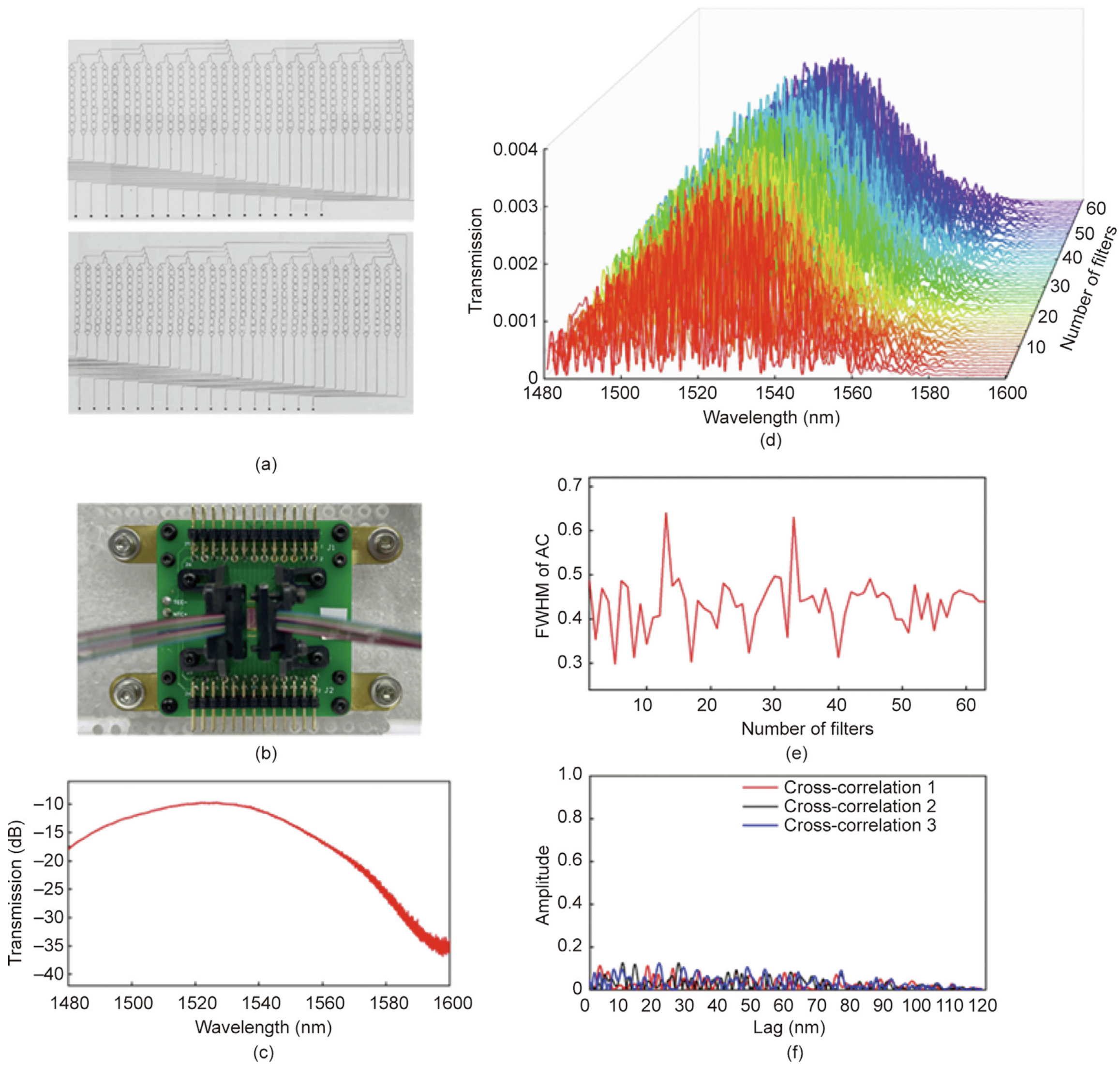

Fig. 4. (a) Microscopic images of structures; (b) photo of packaged chip; (c) measured transmission spectrum of straight waveguide; (d) three-dimensional plot of 64-channel transmission spectra; (e) FWHM of each channel's AC; (f) exemplar CCs of some channels' spectra.

reconstructed with a 0.2 nm FWHM, whereas the passband at 1580 nm exhibited greater distortion owing to the strong ripples and low transmission caused by the band edge of the grating couplers. However, the correct position of the wavelength was accurately captured. To further demonstrate the capabilities of the spectrometer, we sent two reflection spectra with 25 and 10 nm bandwidths from the two chirped FBG for reconstruction, as shown in Fig. 5(b). These results confirm the ability of the spectrometer to accurately reconstruct the broadband components.

To demonstrate the practical application of our spectrometer, we used it as a spectrum analyzer for an FBG sensor. FBG can be employed as sensors such as for temperature sensing, strain sensing, structural monitoring, and fire alarms by tracking the shift of its passband caused by environmental changes. Therefore, a high-resolution broadband spectrometer is required to accurately track the spectral shifts within a broad optical range. We intentionally caused a spectral shift to a 0.2 nm-wide FBG by either increasing the surrounding temperature or applying stress. The results are depicted in Figs. 5(c) and (d), revealing that the spectrometer can resolve a small change of 0.2 nm. This demonstrates the potential of our spectrometer for use in conjunction with FBG in various sensing applications, such as temperature, stress, and fire sensors.

Although sparse spectral reconstruction is a well-known application of computational spectroscopy, the ability of our spectrometer to reconstruct dense spectra is an important aspect of its capabilities. To evaluate the performance of our spectrometer, we reconstructed the transmission spectra of the FBG, which exhibited a narrow notch in the spectrum. The spectra first pass through an optical bandpass filter with a bandwidth of over 35 nm and then enter the spectrometer. As expected, the reconstruction of such a dense spectrum presents a greater challenge; the results are shown in Figs. 5(e) and (f). Although the reconstruction accuracy was lower than that of the sparse spectra, we observed that the spectrum with a 1 nm-wide notch could still be accurately reconstructed. Even a parasitic side notch with shorter wavelength can be captured. This suggests that our spectrometer can accurately detect and quantify the features of the dense spectra, although it has some limitations. Nonetheless, most natural spectra containing useful information are typically smooth and sparse; therefore, the potential applications of our spectrometer remain extensive.

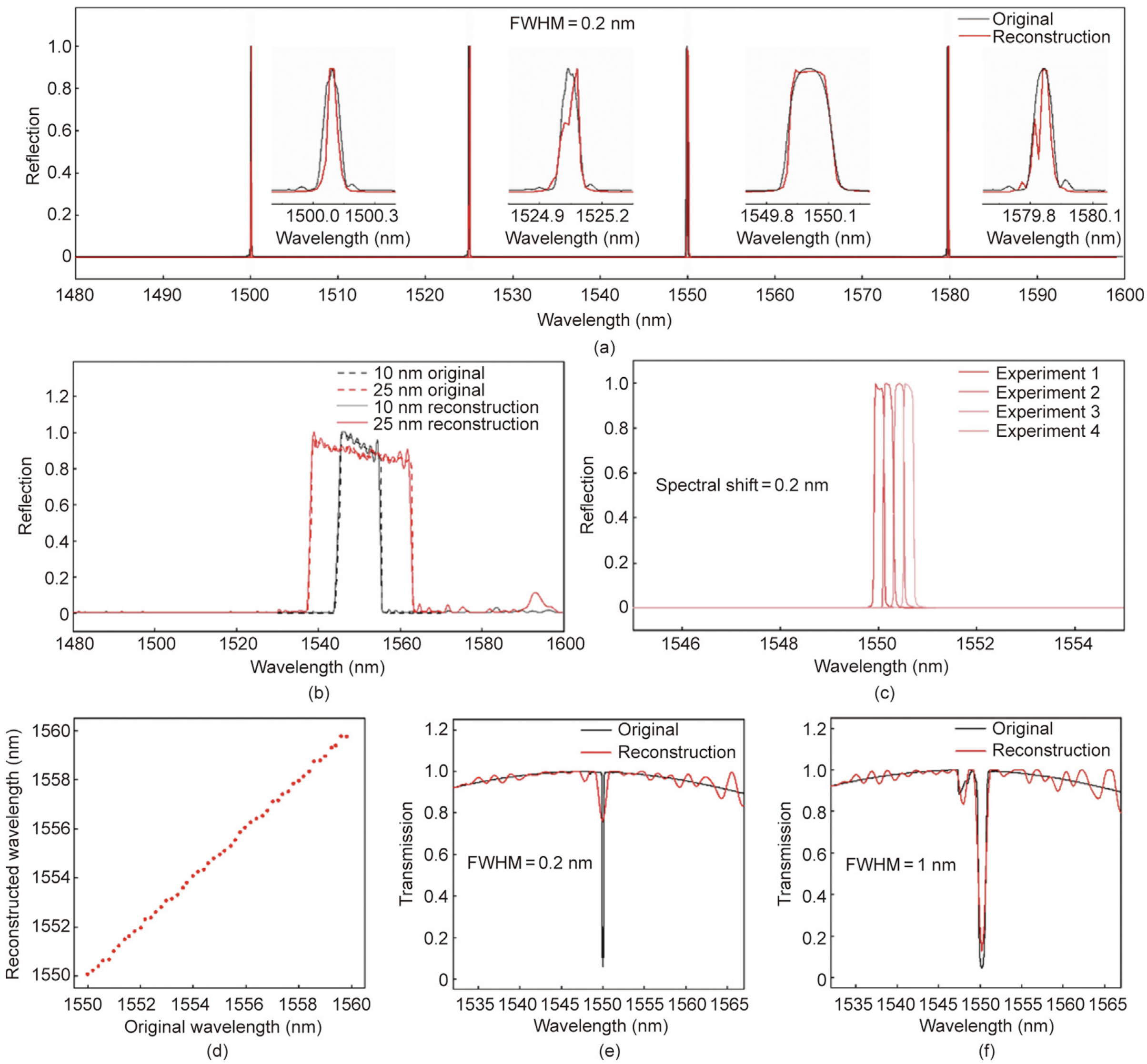

Fig. 5. Spectrum reconstruction results. (a) Four reflection spectra with 0.2 nm wide passband from FBGs are successfully reconstructed; (b) two broadband spectra from chirped FBG successfully reconstructed; (c, d) spectral shift of FBG as small as 0.2 nm tracked by our spectrometer; (e, f) transmission spectra of two FBG with 1 nm FWHM and 0.2 nm FWHM tested for reconstruction.

4. Discussion

We established and validated a reliable inverse design method for high-performance CSSS. Using this method, a spectrometer that leveraged a novel disordered photonic chip based on interferometric effects was developed on a silicon photonic platform. Unlike previous approaches that employed a brute-force random design method for disordered photonic media, we utilized a bioinspired inverse design algorithm at the system level. This resulted in a significantly improved spectral resolution for each disordered structure along with a reduced CC between any two structures. Experimental characterization confirmed a spectral resolution of 0.2 nm and a bandwidth of 100 nm, limited solely by the measurement equipment and fiber/chip coupling elements. In contrast to recently demonstrated computational spectrometers that exhibit picometer-scale resolution or a bandwidth of hundreds of nanometers, our current demonstration might not reach the same level of performance. However, the primary objective of this study was to introduce a novel inverse design method for computational spectrometers rather than presenting a concrete spectrometer with a specific structure and performance. The application of this inverse design method to other structures can also generate an improvement over the random design approach. Furthermore, the scalability of the spectrometer is exceptional given the absence of inherent bandwidth limitations. The resolution can be further enhanced by modifying the structure of the disordered photonic chip; for instance, by incorporating more coupling points or increasing the maximum delay length differences. We also demonstrate the practical application of our spectrometer as a spectrum analyzer for FBG sensors. Our study signifies a substantial leap forward in the readiness of Si-integrated spectrometers for commercial products, providing high-performance and scalable solutions for a diverse range of applications.

5. Conclusions

A reliable inverse design method for high-performance CSSSs was developed. Using this method, we developed a spectrometer featuring a novel disordered photonic chip based on interferometric effects integrated into a silicon photonic platform. This approach results in a significantly improved spectral resolution and reduced CC between structures. This method can also be applied to other structures, potentially offering improvements over random approaches. We also demonstrated the practical application of our spectrometer as a spectrum analyzer for FBG sensors. This study represents a significant advancement in the readiness of Si-integrated spectrometers for commercial products, providing high-performance and scalable solutions for a diverse range of applications.

Compliance with ethics guidelines

Ang Li, Yifan Wu, Gongyuan Zhang, Chang Wang, Jijun He, Yaqi Shi, Zongyin Yang, and Shilong Pan declare that they have no conflict of interest or financial conflicts to disclose.

Acknowledgments

This work was supported by National Key Research and Development Program of China (2021YFB2801500, 2022YFB3206001, and 2023YFB3405600), National Natural Science Foundation of China (62375126, 62105149, and 62334001), the Leading Innovation and Entrepreneurship Team Project in Zhejiang (2022R01001), Key Laboratory of Modern Optical Technologies of Education Ministry of China, Soochow University, and State Key Laboratory of Advanced Optical Communication Systems and Networks, China.

Appendix A. Supplementary data

Supplementary data to this article can be found online at https://doi.org/10.1016/j.eng.2024.07.011.

References

[1] Yang Z, Albrow-Owen T, Cai W, Hasan T. Miniaturization of optical spectrometers. Science 2021;371(6528):eabe0722.
[2] Li A, Yao C, Xia J, Wang H, Cheng Q, Penty R, et al. Advances in cost-effective integrated spectrometers. Light Sci Appl 2022;11:174.
[3] Xiao Z, Liu W, Xu S, Zhou J, Ren Z, Lee C. Recent progress in silicon-based photonic integrated circuits and emerging applications. Adv Opt Mater 2023;11(20):2301028.
[4] Ma K, Chen K, Zhu N, Liu L, He S. High-resolution compact on-chip spectrometer based on an echelle grating with densely packed waveguide array. IEEE Photonics J 2019;11(1):4900107.
[5] Ma X, Li M, He JJ. CMOS-compatible integrated spectrometer based on echelle diffraction grating and MSM photodetector array. IEEE Photonics J 2013;5(2):6600807.
[6] Xia Z, Eftekhar AA, Soltani M, Momeni B, Li Q, Chamanzar M, et al. High resolution on-chip spectroscopy based on miniaturized microdonut resonators. Opt Express 2011;19(13):12356–64.
[7] Redding B, Liew SF, Sarma R, Cao H. Compact spectrometer based on a disordered photonic chip. Nat Photonics 2013;7(9):746–51.
[8] Bao J, Bawendi MG. A colloidal quantum dot spectrometer. Nature 2015;523(7558):67–70.
[9] Wang Z, Yi S, Chen A, Zhou M, Luk TS, James A, et al. Single-shot on-chip spectral sensors based on photonic crystal slabs. Nat Commun 2019;10:1020.
[10] Zhu X, Bian L, Fu H, Wang L, Zou B, Dai Q, et al. Broadband perovskite quantum dot spectrometer beyond human visual resolution. Light Sci Appl 2020;9:73.
[11] Boschetti A, Taschin A, Bartolini P, Tiwari AK, Pattelli L, Torre R, et al. Spectral super-resolution spectroscopy using a random laser. Nat Photonics 2020;14(3):177–82.
[12] Li A, Fainman Y. On-chip spectrometers using stratified waveguide filters. Nat Commun 2021;12:2704.
[13] Hadibrata W, Noh H, Wei H, Krishnaswamy S, Aydin K. Compact, high-resolution inverse-designed on-chip spectrometer based on tailored disorder modes. Laser Photonics Rev 2021;15(9):2000556.
[14] Gao L, Qu Y, Wang L, Yu Z. Computational spectrometers enabled by nanophotonics and deep learning. Nanophotonics 2022;11(11):2507–29.
[15] Chang Y, Xu S, Dong B, Wei J, Le X, Ma Y, et al. Development of triboelectric-enabled tunable Fabry-Pérot photonic-crystal-slab filter towards wearable mid-infrared computational spectrometer. Nano Energy 2021;89:106446.
[16] Liu X, Liu W, Ren Z, Ma Y, Dong B, Zhou G, et al. Progress of optomechanical micro/nano sensors: a review. Int J Optomechatronics 2021;15(1):120–59.
[17] Wu L, Cai Z, Su Y, Wu J. Simulative study on speckle's spectral properties of a random pixelated grating. J Opt Soc Am A Opt Image Sci Vis 2019;36(8):1410–7.
[18] Lin Z, Yu S, Chen Y, Cai W, Lin B, Song J, et al. High-performance, intelligent, on-chip speckle spectrometer using 2D silicon photonic disordered microring lattice. Optica 2023;10(4):497–504.
[19] Li A, Wang C, Bao F, Fang W, Liang Y, Cheng R, et al. An integrated single-shot spectrometer with large bandwidth-resolution ratio and wide operation temperature range. PhotoniX 2023;4:29.
[20] Fu PH, Chao CY, Huang DW. Ultracompact silicon waveguide bends designed using a particle swarm optimization algorithm. IEEE Photonics J 2021;13(1):6600509.
[21] Mak JCC, Sideris C, Jeong J, Hajimiri A, Poon JKS. Binary particle swarm optimized 2 × 2 power splitters in a standard foundry silicon photonic platform. Opt Lett 2016;41(16):3868–71.
[22] Zagaglia L, Floris F, O'Brien PA. Experimental characterization of particle swarm optimized focusing non-uniform grating coupler for multiple SOI thicknesses. J Lightwave Technol 2021;39(15):5028–34.
[23] Chen W, Li H, Zhang B, Wang P, Dai S, Liu Y, et al. Silicon mode (de) multiplexer based on cascaded particle-swarm-optimized counter-tapered couplers. IEEE Photonics J 2020;13(1):6600210.
[24] Abedi K, Mirjalili SM. Slow light performance enhancement of Bragg slot photonic crystal waveguide with particle swarm optimization algorithm. Opt Commun 2015;339:7–13.
[25] Djavid M, Mirtaheri S, Abrishamian M. Photonic crystal notch-filter design using particle swarm optimization theory and finite-difference time-domain analysis. J Opt Soc Am B 2009;26(4):849–53.
[26] Zhang Y, Yang S, Lim AEJ, Lo GQ, Galland C, Baehr-Jones T, et al. A compact and low loss Y-junction for submicron silicon waveguide. Opt Express 2013;21(1):1310–6.
[27] Kennedy J, Eberhart R. Particle swarm optimization. In: Proceedings of International Conference on Neural Networks; 1995 Nov 27–Dec 1; Perth, WA, Australia; 1995.
[28] Guimaraes DA, Floriano GHF, Chaves LS. A tutorial on the CVX system for modeling and solving convex optimization problems. IEEE Latin Am T 2015;13(5):1228–57.
[29] Zhang J, Zhu X, Bao J. Denoising autoencoder aided spectrum reconstruction for colloidal quantum dot spectrometers. IEEE Sens J 2020;21(5):6450–8.
[30] Zhang J, Zhu X, Bao J. Solver-informed neural networks for spectrum reconstruction of colloidal quantum dot spectrometers. Opt Express 2020;28(22):33656–72.